Chemical Engineering Journal 497 (2024) 154607

Contents lists available at ScienceDirect

Chemical Engineering Journal

journal homepage: www.elsevier.com/locate/cej

Microenvironment design strategies for enhanced CO_2 electroreduction with a 60% full-cell energy efficiency

Pengtao Yue [a,b], Junjun Wu [a,b], Chaozhong Qin [c,d], Bowen Shi [c,d], Yang Wang [a,b], Yue Zhang [a,b], Yanan Zou [a,b], Jun Li [a,b], Liang Zhang [a,b], Xun Zhu [a,b], Miao Zhong [e], Qian Fu [a,b,*], Qiang Liao [a,b,*]

[a] Key Laboratory of Low-grade Energy Utilization Technologies and Systems, Chongqing University, Ministry of Education, Chongqing 400044, China
[b] Institute of Engineering Thermophysics, School of Energy and Power Engineering, Chongqing University, Chongqing 400044, China
[c] State Key Laboratory of Coal Mine Disaster Dynamics and Control, Chongqing University, Chongqing 400044, China
[d] School of Resources and Safety Engineering, Chongqing University, Chongqing 400044, China
[e] College of Engineering and Applied Sciences, National Laboratory of Solid State Microstructures, Collaborative Innovation Center of Advanced Microstructure, Jiangsu Key Laboratory of Artificial Functional Materials, Nanjing University, Nanjing, China

ARTICLE INFO

Keywords:
Electrochemical CO_2 reduction
Ni single atom catalyst
Catalyst layer
Mass transport

ABSTRACT

Low current densities (production rates) and low energy efficiency (EE) caused by poor catalyst activities and limited CO_2 mass transfer in the catalyst layer (CL) prevent CO_2 electrolysis from application. Herein, we report atomically dispersed Ni catalysts anchored on macroporous hollow nano-carbon sheets (A-Ni@CS) that simultaneously optimizes the coordination of Ni atoms and CO_2 transport in the CL. The unique Ni–N_5–O/C structure of A-Ni@CS lowers the energy barrier of *COOH formation, and the layered nano-to-micro porous structure increases the mass transfer of CO_2, enhancing the local CO_2 concentration in the CL. By employing a zero-gap flow cell, A-Ni@CS can mediate CO_2 to CO conversion with a 60 % full-cell EE at 200 mA/cm^2.

1. Introduction

Electrochemical CO_2 reduction reaction (CO_2RR) integrated with renewable energy is an attractive approach for mitigating greenhouse gas emissions and converting CO_2 to value-added chemicals [1–4]. Electrochemical reduction of CO_2 to CO is a practical method for reducing greenhouse gas emissions owing to the high selectivity and large market demand of CO [5–8]. Efforts toward the exploration of high-performance CO_2RR catalysts (*e.g.*, Au [9], Ag [10], and Ni single-atom catalysts (Ni SAC) [11]) have demonstrated that near-unity faradaic efficiency of CO (FE_{CO}) can be achieved. Improvements in the full-cell energy efficiency (EE, >60 %) [12] of CO at an industrially relevant current density (>200 mA/cm^2) [13] is the major priority for the commercial application.

Ni based materials (*e.g.,* Ni SACs) demonstrate significant activity, selectivity, and maximum atom efficiency [14–20]. However, it is challenging to construct excellent Ni SACs with high EE and high current densities because most of them have a parallelogram structure (Ni–N_4) that limits electron transfer owing to symmetric charge distribution [18]. The introduction of a coordinating axial ligand to Ni–N_4 can modulate the *d*-electron states of metal centers; thus, this method is regarded as an efficient approach for optimizing the dynamic activation of the CO_2RR [11].

The CO_2RR is typically performed in conventional H-cells with a current density of < 50 mA/cm^2 because of the low solubility (33 mM at room temperature) [21] and insufficient local concentration of CO_2 in an aqueous electrolyte. A zero-gap flow cell employing a gas diffusion electrode (GDE) deposited with catalysts can overcome the mass-transfer limitation by directly delivering gaseous CO_2 to participate in the CO_2RR, greatly improving the local CO_2 concentration and enhancing the CO_2RR activity [22]. Therefore, apart from the intrinsic activity of the catalysts, the local CO_2 concentration in the catalyst layer (CL), significantly impacts the performance toward CO_2 electrolysis, especially when the CL is partially flooded with an aqueous electrolyte [23].

Current studies tend to focus on the design of catalysts with high

* Corresponding authors at: Key Laboratory of Low-grade Energy Utilization Technologies and Systems, Chongqing University, Ministry of Education, Chongqing 400044, China.

E-mail addresses: fuqian@cqu.edu.cn (Q. Fu), lqzx@cqu.edu.cn (Q. Liao).

https://doi.org/10.1016/j.cej.2024.154607
Received 27 March 2024; Received in revised form 24 June 2024; Accepted 5 August 2024
Available online 10 August 2024

intrinsic activity but ignore the significance of local CO_2 concentration in the CL [24,25]. Improving the local concentration of CO_2 within the CL offers a promising approach to foster the development of highly enriched three-phase reaction interfaces. This augmentation significantly enhances the CO_2RR activity, particularly when operating at industrial current densities. When the CL pore sizes are comparable or smaller than the mean free path (MFP) of CO_2 molecules (84 nm at room temperature) [26], mixed diffusion (*i.e.*, Knudsen and bulk diffusion) determines mass transport in the CL. In contrast to bulk diffusion (which occurs when the pore size of the CL is much larger than the MFP of CO_2 molecules), CO_2 molecules frequently collide with the pore wall depending on Knudsen diffusion and exponentially decrease the diffusivity coefficient (D_{eff}/D_0, D_{eff} represents the effective diffusivity coefficient and D_0 represents the molecular diffusivity coefficient) of CO_2 molecules, reducing the local CO_2 concentration in the CL and decreasing the performance. In addition, the saturation of the gas phase within the CL also exerts a significant influence on the local CO_2 concentration, particularly when the CL experiences partial flooding with an aqueous electrolyte.

Herein, we prepare a Ni SAC anchored on a macroporous hollow nano-carbon sheet (A-Ni@CS) to modulate the d-electron states of Ni centers and optimize the dynamic activation of the catalyst through introducing coordinating axial N and O to Ni–N_4, which can simultaneously increase the local CO_2 concentration in the CL by enhancing the D_{eff}/D_0 of CO_2. X-ray characterization studies [X-ray diffraction (XRD), X-ray photoelectron spectroscopy (XPS), and X-ray absorption spectroscopy (XAS)] and density functional theory (DFT) calculations were employed to investigate the electronic structure of A-Ni@CS and its dynamic activation for the CO_2RR. Tomographic reconstruction and pore-network modeling (PNM) analysis of the CL were conducted to explore the D_{eff}/D_0 of the CO_2 molecules and their local concentration in the CL. Through the microenvironment design strategies, we demonstrate that the prepared A-Ni@CS exhibits higher full-cell EE under the same current density than that achieved using recently developed state-of-the-art catalysts. This work highlights the importance of tailoring the CL microenvironment as a means of improving the overall performance in the CO_2RR, and offers a unique insight to drive industrial applications of current systems.

2. Methods

2.1. Chemicals and materials.

Sodium citrate dihydrate ($Na_3C_6H_5O_7{\cdot}2H_2O$, >99 %), hydrochloric acid (HCl, 36–38 %), potassium bicarbonate ($KHCO_3$, >99.5 %), potassium hydroxide (KOH, >90 %), potassium thiocyanate (KSCN, >98.5 %), and potassium chloride (KCl, >99.5 %) were purchased from Kelong (Chengdu, China). Ethanol (C_2H_5OH, >99.7 %) and urea (NH_2CONH_2, >99 %) were purchased from Shanghai Titan Scientific Co., Ltd. Nickel (II) acetate tetrahydrate ($Ni(OCOCH_3)_2{\cdot}4H_2O$, 99 %, Ni > 23 %) was purchased from Alab (Shanghai) Chemical Technology Co., Ltd. 1, 10-Phenanthroline monohydrate ($C_{12}H_8N_2{\cdot}H_2O$, 98 %) was purchased from Shanghai Macklin Biochemical Co., Ltd. Nafion 117 solution (5 wt %) was obtained from Sigma-Aldrich. CB (Vulcan XC-72R), carbon paper (Freudenberg H14C9), Sustainion XA-9 ionomer solution (5 wt%), and Sustainion® X37-50 Grade T anionic exchange membrane were purchased from Fuel Cell Store. Deionized water (18.25 MΩ·cm) was obtained from an Antesheng system.

2.2. Synthesis

Porous hollow nano-CS was synthesized through high-temperature pyrolysis. First, sodium citrate dehydrate was dried in an oven at 160 °C overnight. The obtained sample was ground into powder using a mortar and pestle and subsequently delivered to the tube furnace (SKG08123K-610, Tianjin, China). Then, the white solid was heated to 900 °C at a rate of 1 °C /min and maintained at 900 °C for 3 h under N_2 atmosphere (99.999 %). The obtained black solid after cooling to room temperature was cleaned with hydrochloric acid, ethanol, and deionized water for several times to remove the impurities. Finally, the black powder was denoted as CS.

By combining different types of polymer with oxides and carbon-based materials the new composites with increased and attractive electronic properties could be fabricated [27]. In this study, to anchor Ni single-atom catalysts on CS, nickel (II) acetate tetrahydrate (12.4 mg) and 1, 10-phenanthroline monohydrate (29.7 mg) were first mixed in ethanol (2 mL), and the solution was stirred (800 rpm) for 30 min. Then, CS (69.6 mg) was added into this solution by stirring for 30 min (800 rpm). The final solution was transferred into a water bath and heated to 60 °C for 4 h and dried at 80 °C for 24 h in an oven. The obtained black solid was heated to 600 °C at a rate of 10 °C/min, and maintained at 600 °C for 2 h under the N_2 atmosphere in the tube furnace. After cooling down to room temperature, the black solid was mixed with urea (1:10) and ground using a mortar and pestle. At last, the mixture was heated to 800 °C at a rate of 5 °C /min, and held at 800 ℃ for 1 h (N_2 atmosphere). The obtained product after cooling was washed with hydrochloric acid (80 °C, 12 h) to remove the Ni nano-particles. The final black solid was denoted as A-Ni@CS. Additionally, A-Ni@CB was synthesized using the same method except replacing the CS with commercial CB.

2.3. Electrode preparation.

The prepared catalysts (A-Ni@CS or A-Ni@CB) were dispersed into a mixed solution (0.5-mL ethanol, 0.5-mL deionized water, and 20-μL Nafion solution (5 wt%)) and then sonicated for 30 min to obtain a uniform catalyst ink. The carbon paper was washed with deionized water and ethanol for several times before being used. Next, 200-μL catalyst ink was dropped onto a hydrophobic carbon paper (1 cm^2) for the H-cell test. For electrochemical tests performed in a zero-gap flow cell with a membrane electrode assembly (MEA), 20-mg catalysts, 200-μL ionomer solution (*i.e.*, Nafion and Sustainion), and 5-mL ethanol were mixed and then air-brushed onto the carbon paper using a spray gun toward a catalyst concentration of 1 mg/cm^2. The results confirm that Nafion-coated catalyst has a better catalytic performance than that of Sustainion-coated catalyst (Supplementary Fig.13) due to the Nafion-coated catalyst are more hydrophobic. Nafion-coated A-Ni@CS has a higher contact angle (140°) than that of Sustainion-coated A-Ni@CS (53°), as shown in Supplementary Fig.15 and Fig.27. A hydrophobic surface probably can form more triple-phase interfaces and trap gaseous CO_2 at the catalyst surface, increasing the CO_2 concentration at the electrode–electrolyte interface and enhancing the electrochemical performance for the CO_2RR.[21] A hydrophilic surface probably induce water flooding within the electrode, blocking the transport channels of CO_2 and destroying the triple-phase interfaces. Although a hydrophilic surface can provide more water during electrolysis, the triple-phase interfaces are probably destroyed due to the water flooding. Thus, all experiments were conducted using Nafion-coated catalysts. The thickness of the CL was measured by capturing the cross-section SEM images, as shown in Supplementary Fig.24 and Fig. 26. The thickness of A-Ni@CS and A-Ni@CB CLs with a 1 mg/cm^2 catalyst loading are around 86 ± 4 μm and 10 ± 3 μm, respectively.

2.4. Electrochemical measurements.

For electrochemical tests performed in a customized H-cell, a cation exchange membrane (UltrexCMI-7000, Membranes International Inc., Ringwood, NJ, USA) was used to separate the cathode and anode chambers. The traditional three-electrode system was selected during the CO_2RR. A Ag/AgCl electrode (saturated with KCl), a Pt foil (1 cm^2), and an electrode holder with the prepared catalysts were used as the reference electrode, counter electrode, and working electrode, respectively. The two chambers were filled with $KHCO_3$ solution (0.1 M); this

solution should be saturated with N_2 or CO_2 (99.999 %, >30 min) before tests. Then, an electrochemical workstation (ParSTAT MC, Princeton, USA) was carried out to perform the electrochemical tests. Specifically, the LSV test was conducted at a scan rate of 20 mV/s in N_2– or CO_2-saturated $KHCO_3$ solution (0.1 M). To collect the FE of the products, the working electrode with the prepared catalysts was held at a constant potential for 20 min, and the rate of the CO_2 gas at the inlet was set as 30 sccm using a flow controller (D07-19B, Sevenstar, China). In N_2-saturated $KHCO_3$ solution (0.1 M), cyclic voltammetry (CV) data were collected from − 0.3 to − 0.4 V vs. Ag/AgCl with scan rates of 20, 40, 60, 80, and 100 mV/s to measure the ECSA of the prepared catalysts. In this study, all potentials measured against a Ag/AgCl electrode (saturated with KCl) were converted to the reversible hydrogen electrode (RHE) using E (vs. RHE) = E (vs. Ag/AgCl) + 0.197 + 0.0591 × pH.

When the electrochemical tests were performed in a zero-gap flow cell, a two-electrode system was selected. Ni foam (3 × 3 cm^2) and A-Ni@CS (or A-Ni@CB) catalysts sprayed on carbon paper were used as the anode and cathode, respectively. An anionic exchange membrane (Sustainion® X37-50 Grade T) was sandwiched by the anode (Ni foam) and cathode (carbon-paper-supported catalysts). The membrane should be immersed in KOH solution (1 M) for 24 h before use. Ni foam and carbon paper should be washed with ethanol for 15 min and then cleaned with deionized water for 15 min. During electrolysis, humidified CO_2 was delivered to the cathode by a flow controller with a rate of 100 sccm. KOH solution (1 M) was supplied to the anode at a rate of 20 mL/min using a peristaltic pump. All electrochemical tests were conducted at 25 °C and 1 atm pressure. During the diluted experiments, different standard gas with different concentration of gaseous CO_2 and N_2 was humidified and transported to the cathode. For example, 0.2 partial pressure CO_2 represents that the standard gas mixture is composed of 20 % CO_2 and 80 % N_2. The stoichiometry is 12.5, 16.7, 47.6, 75.8, and 149 for A-Ni@CS when the CO_2 flow rate is 5, 10, 30, 50, and 100 sccm, respectively. Besides, the stoichiometry is 417, 36.1, 52.1, 83.3, and 152.2 for A-Ni@CB when the CO_2 flow rate is 5, 10, 30, 50, and 100 sccm, respectively.

2.5. CO_2RR products analysis.

To quantify the gaseous products (CO and H_2) after electrolysis, the collected gaseous mixture is delivered to a gas chromatograph (GC) (Shimadzu GC-2030, Japan), which is equipped with three detectors (one thermal conductivity detector and two flame ionization detectors). H_2, O_2, and N_2 were quantified through the thermal conductivity detector. CH_4, C_2H_4, CO, and other C2–C3 chemicals (>1 ppm) were detected using two flame ionization detectors with a methanizer. The corresponding partial current density (j_i) was calculated as follows:

$$j_i = j_{total} \times n_i z_i F / Q \times 100\,\%$$

where z_i represents the number of electrons transferred to products (CO or H_2), F is the Faradaic constant (96,485C/mol), n_i (mol) is the mole of products (CO or H_2) after electrolysis, Q (C) is the charge quantity, and j_{total} represents the total current density through the system. The corresponding FE of CO or H_2 was calculated as follows:

$$FE = j_i / j_{total} \times 100\,\%$$

The EE is calculated as follows [5]:

$$EE = FE_{CO} \times E^0 / E_{cell}$$

where E^0 represents the equilibrium potential toward CO production ($E^0 = E^0_{cathode} - E^0_{anode} = -0.11 - 1.23 = -1.34$ V), E_{cell} is the cell voltage potential, and FE_{CO} is the Faradaic efficiency of CO production.

2.6. Material characterizations.

SEM images were taken from a scanning electron microscope (Hitachi-4800, Japan). The cross-sections SEM images of GDE were prepared by cryo-fracturing GDEs in liquid nitrogen. Transmission electron microscopy (TEM) measurements were carried out on a Tecnai G2 F20 microscope operated at 200 kV. The XRD patterns were collected on a BRUCKER D8 X-ray diffractometer. XPS was performed on a Thermo Fisher ESCALAB 250Xi spectrometer. Raman spectroscopy was recorded on a Renishaw Raman microscope through an Ar ion laser (the excitation wavelength is 532 nm). BET analysis was conducted on a TriStar II 3020 analyzer. ICP-MS analysis was performed on an Agilent ICPOES730 series instrument. Atomic-resolution (AC-STEM) images of the catalysts were collected from JEM ARM 200F operated under 200 kV.

The XAS (XANES and X-ray absorption fine structure (EXAFS)) of the synthesized catalysts were collected at the Singapore Synchrotron Light Source (SSLS) center, where a pair of channel-cut Si (1 1 1) crystals was used in the monochromator. The Ni K-edge XANES data were recorded in the transmission mode. Ni foil, NiO, and NiPc were used as the control references. The storage ring was used at the energy of 2.5 GeV with an average electron current of below 200 mA. The acquired EXAFS data were extracted and processed according to the standard procedures using the ATHENA module implemented in the IFEFFIT software packages. The k^3-weighted Fourier transform (FT) of x(k) in R space was obtained over the range of 0–14.0 Å-1 by applying a Besse window function.

FIB-SEM tomography was conducted on Helios NanoLab-650 (FEI, USA). First, a device (Leica EM TXP, Germany) was used for milling, sawing, grinding, and polishing a piece of sample (GDE). Then, argon ion polishing was performed on the surface of the prepared sample by a polishing machine (Leica RES 102, Germany). The voltage and current of the two ion guns were set as 5 kV and 2.2 mA, respectively. During polishing (4 h), the angle of inclination was 2°. The obtained area of the sample was approximately 1 cm^2. Finally, the surface of the GDE was plated with a layer of carbon using a carbon sputter coater (EMITECH K950X, England) with a 2-mm long carbon rod. The resolution in the milling direction was 6 nm. The image size in the SEM plane of A-Ni@CB and A-Ni@CS CLs were 2048*1768 and 1024*884, respectively. The voxel size of A-Ni@CB and A-Ni@CS CLs were 6 nm*6 nm*6 nm.

2.7. DFT computational details.

All DFT calculations were performed by using the VASP code [28]. The inner cores of the atom were replaced by the frozen-core approximations. The projector-augmented wave (PAW) method was applied to describe the electron − core interaction [29]. The Perdew–Burke–Ernzerhof (PBE) functional within the generalized gradient approximation (GGA) was used to model the exchange correlation energy [30]. A Hubbard U correction of 3.40 eV for Ni atoms was added in all calculations [31]. The cutoff energies for plane waves were set to 520 eV. The spin-polarization effect was employed in all calculations. Geometry optimizations were performed by using the conjugate gradient algorithm until all forces became smaller than 0.02 eV/Å. Self-consistent-field (SCF) was performed with an electronic structure iteration of 1 × 10 − 5 eV on the total energy. The k-point sampling of the Brillouin zone was obtained using a 3 × 3 × 1 grid for the repetitive unit by the gamma centered Monkhorst-Pack scheme. A Gaussian smearing with σ = 0.05 eV to the orbital occupation is employed during structure relaxation and energy calculations. A vacuum slab of 15 Å was inserted in the z-direction for all models to avoid the influence of the interaction between adjacent periodic units. The DFT-D3 method with Becke–Jonson damping was used for vdW corrections in geometry optimizations and total energy calculations [32,33].

2.8. Pore-network modeling details.

We used the FIB-SEM technique to obtain the 3D images of the A-Ni@CS and A-Ni@CB catalyst layers (CLs), which were further

segmented into pore spaces and solid phase. We used the open source software PoreSpy [34] to extract the pore-network information of the constructed 3D porous structures, including volumes, inscribed radii, and surface areas of discrete pore spaces. The pore spaces were idealized by three types of pore elements in our in-house quasi-static pore-network model, namely, tubes of circular, square, and triangular cross-sections [35]. The shape of the pore elements is calculated based on its shape factor [36] and the equation is shown as follows:

$$G = A/P^2$$

Where G is the shape factor, A is the sectional area of the tube (m^2), and P is the sectional perimeter of the tube (m). The shape factors of circular, square, and triangular cross-sections are $\frac{\sqrt{3}}{36}$, $\frac{\pi}{4}$, and $\frac{1}{16}$, respectively.

We conducted a Direct Numerical Simulation (DNS) of CO_2 molecular diffusion in the CLs to verify the results obtained by PNM. Then, the quasi-static PNM was used in the two-phase flows due to its high computational efficiency. The DNS exhibits that the effective diffusivity coefficients of CO_2 (only considering molecular diffusion in the verification) in the A-Ni@CS CL along the x, y, and z directions are 0.55, 0.69, and 0.59, respectively, indicating the homogeneity of the porous structures model. The effective diffusivity coefficient of CO_2 in the A-Ni@CS CL along z direction by the PNM is 0.73, which is close to the DNS prediction. Additionally, we also calculated the effective diffusivity coefficients of CO_2 in the A-Ni@CB CL, which is 0.11, 0.10, and 0.16, respectively, along the x, y, and z directions. The PNM results show that the effective diffusivity coefficient of CO_2 (only considering molecular diffusion in the verification) in the A-Ni@CB CL along z direction is 0.18, which is also close to the DNS prediction. These results confirm the reliability of the method for molecular diffusion. In subsequent PNM simulations, the Knudsen effect is incorporated. Although the PNM result is a qualitative analysis, it can still reflect the effect of pore structure on CO_2 transport.

We simulated the primary drainage process, in which liquid water invaded the dry media following the invasion-percolation algorithm. We put the nonwetting reservoir of liquid water at the inlet, and the wetting reservoir of air at the outlet. The inlet water pressure was increased step by stepwise so that only one pore throat could be invaded at each step. Meanwhile, we solved the steady-state diffusion equation (Fick's first law) inside each phase, which was given as:

$$\sum_{j=1}^{N_i} D_{ij} A_{ij} \frac{C_i - C_j}{L_{ij}} = 0$$

where subscripts i, j, and ij denoted the two connected pore bodies and their pore throat, N_i is the coordinate number of pore body i, D ($\frac{m^2}{s}$) is diffusivity, A [m^2] is the diffusion area of either phase, c is the species concentration, and L [m] is the diffusion length between the two pore bodies.

The CLs had nanoscale pores, and thus, we consider the Knudsen diffusion as follows:

$$D_{KA} = \frac{du}{3} = \frac{d}{3}\sqrt{\frac{8RT}{\pi M_A}}$$

where D_{KA} is the Knudsen diffusivity,d is the diameter of a pore element,R is the ideal gas constant,T is the temperature in kelvins,M_A is the molar mass.

The diffusivity of CO_2 in a pore body was calculated by:.$\frac{1}{D_{Ae,i}} = \frac{1}{D_{AB,i}} + \frac{1}{D_{KA,i}}$

Overall, the effective diffusivity between pore body i and j is given by the harmonic average:

$$\frac{1}{D^{eff}_{Ae,ij}} = \frac{1}{D_{Ae,i}} + \frac{1}{D_{Ae,ij}} + \frac{1}{D_{Ae,j}}$$

The Dirichlet boundary conditions were imposed at the inlet and outlet, while no flux was imposed at the remaining part. Once the concentration field was available, we used the Fick's law to calculate the effective diffusivity as $D^{eff} = Q^{in}\frac{d}{S(C^{in}-C^{out})}$, where Q^{in} [$\frac{kg}{s}$] is the inlet mass flux given by the PNM, c^{in} and c^{out} are the inlet and outlet species concentrations, respectively. S [m^2] is the area of the inlet face, and d [m] is the sample length. Notice that the effective diffusivity in the water phase was zero before water breakthrough at the outlet. The liquid contact angle was set as 140°.

3. Results and discussion

3.1. Preparation and characterizations of catalysts.

A macroporous hollow nano-CS (Supplementary Fig. 1a–d) was first prepared through facile carbonization under N_2 protection. Ni SACs were synthesized by pyrolyzing a mixture of CS, nickel (II) acetate tetrahydrate, 1,10-phenanthroline monohydrate, and urea (details in the Methods section). The obtained catalysts (A-Ni@CS) maintained the morphology of the initial CS, forming interconnected hollow macropores (Fig. 1a–b; Supplementary Figs. 2–3). Numerous mesopores (2–50 nm) were detected on the catalyst walls, which interconnect the macropores (>50 nm) and could facilitate CO_2 diffusion during the CO_2RR. A lattice distance of 0.34 nm was identified through high-resolution TEM (HRTEM) (Fig. 1c); this distance is ascribed to the (0 0 2) plane of partially graphitized carbon [18]. Fig. 1d–e exhibits the elemental mapping and confirms the uniform distribution of Ni, N, and O species in the CS matrix materials. Aberration-corrected high-angle annular dark-field scanning transmission electron microscopy (HAADF-STEM) of A-Ni@CS was conducted to demonstrate the existential form of Ni in A-Ni@CS. The uniformly dispersed single Ni atoms appear as bright spots (with the atomic diameters of ~ 0.2 nm, which are close to that of a single Ni atom [18]) across the entire CS framework (Fig. 1f–g; Supplementary Fig. 4). For comparison, commercial carbon black (CB) (Supplementary Fig. 5) decorated with Ni SACs (A-Ni@CB) was prepared employing the same method as that used for fabricating (A-Ni@CS). The morphological and structural images (Supplementary Figs. 6–9) of A-Ni@CB demonstrate a high dispersion of CB-anchored atomic Ni.

The XRD patterns of A-Ni@CS (Fig. 1h) exhibit the (0 0 2) and (1 0 1) diffraction patterns of carbon materials at ~ 25.8° and 43.1°, respectively. No distinct metallic Ni was detected in the XRD patterns (Fig. 1h; Supplementary Fig. 10), probably because of its low Ni concentration. XPS was conducted to determine the surface chemical states and elemental compositions of the prepared catalysts (Fig. 1i; Supplementary Fig. 10). High-resolution Ni 2p XPS spectra of A-Ni@CS and A-Ni@CB exhibit Ni $2p_{3/2}$ binding energies located at 855.7 and 855.8 eV, respectively, which are more positive than that of metallic Ni (852.6 eV) [6], confirming that the Ni single atoms in the CS and CB materials are likely to be in positive oxidation states.

3.2. Electrochemical CO_2 reduction.

To explore the electrochemical activity of the prepared catalysts for the CO_2RR, a conventional H-cell (Supplementary Fig. 11) was employed, and a N-doped CS (N-CS) without Ni single atoms was chosen as a reference. Fig. 2a shows the linear sweep voltammetry (LSV) curves of all prepared samples in the CO_2-saturated $KHCO_3$ solution. A-Ni@CS showed higher current densities than those of A-Ni@CB and N-CS, revealing its enhanced activity for the CO_2RR. A-Ni@CS has a low onset overpotential (~290 mV) and a high FE_{CO} of > 90 % at a wide potential

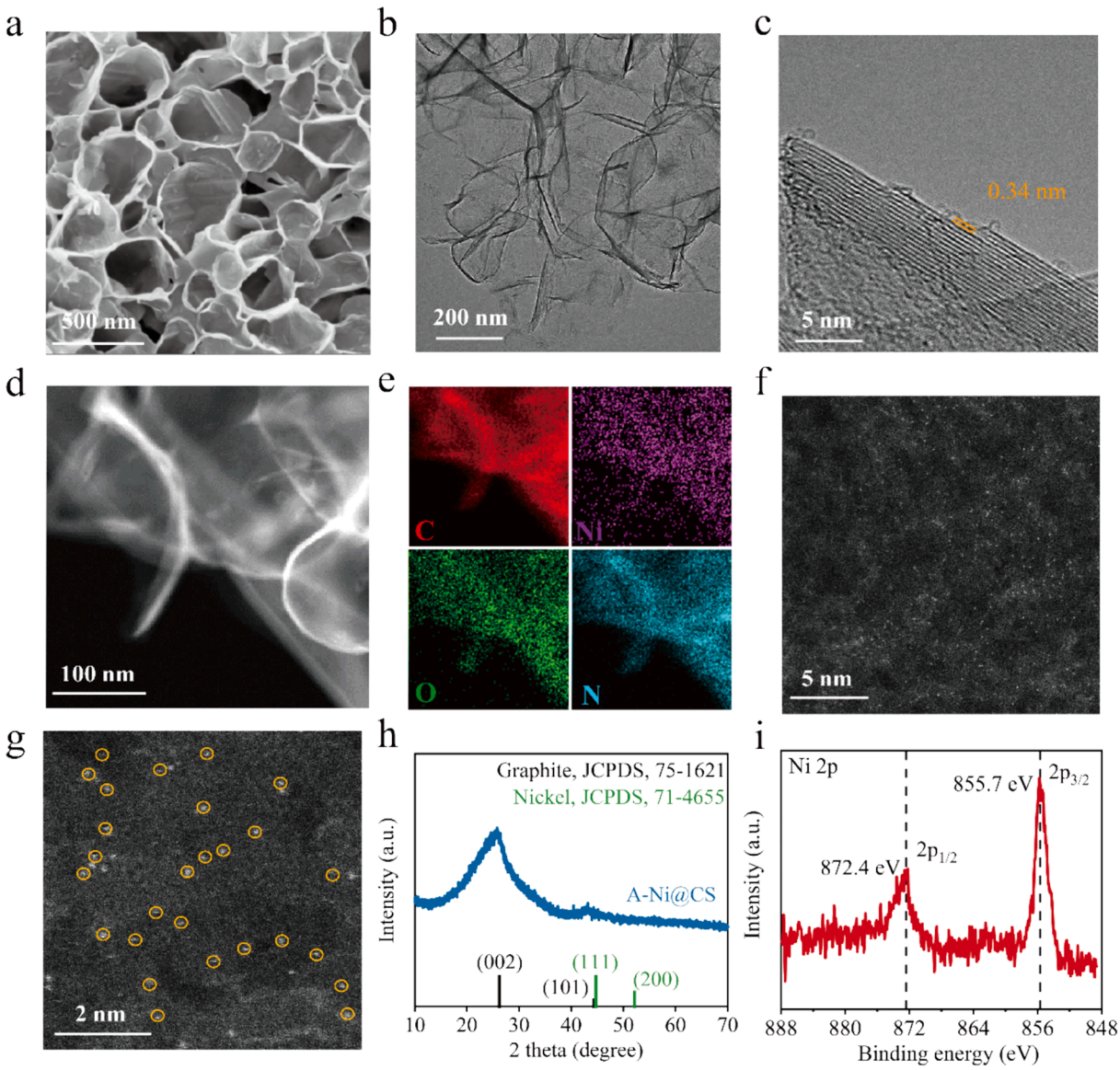

Fig.1. Morphological and structural characterization of A-Ni@CS. (a) High-resolution SEM, (b) TEM, and (c) HRTEM images. (d, e) Elemental mappings. (f) Aberration-corrected HAADF-STEM image and (g) corresponding enlarged HAADF-STEM image. (h) XRD patterns. (i) High-resolution Ni 2p XPS spectra.

ranging from − 0.6 to − 1.4 V vs. RHE (the corresponding FE of H_2 is < 13 %; Fig. 2b–c). The highest FE_{CO} was achieved at − 0.9 V vs. RHE (FE_{CO}=96.2 %). N-CS exhibited low activity toward CO production (<40 %), which confirms that the Ni single atoms greatly influence CO production. The partial current density of CO (j_{CO}) of A-Ni@CS reaches 15.9 mA/cm^2 at − 1.3 V vs. RHE, which is higher than or comparable to those achieved with most state-of-the-art CO-selective electrocatalysts (Fig. 2d; Supplementary Table S1). In contrast, at − 1.3 V vs. RHE, the j_{CO} of A-Ni@CB and N-CS are 14.2 and 2.4 mA/cm^2, respectively.

A-Ni@CS possesses the highest double layer capacitance (C_{dl}) of 9.26 mF cm^{-2} among all samples (A-Ni@CB: 7.59 mF cm^{-2}; N-CS: 5.71 mF cm^{-2}), suggesting its highest electrochemical active surface area (ECSA) (Fig. 2e; Supplementary Fig. 12 h–j). This difference in the ECSA can be attributed to the presence of abundant hierarchical macropores and the larger Brunauer Emmett Teller (BET) surface area (341.5 m^2/g) of A-Ni@CS than that of A-Ni@CB (234.3 m^2/g) (Supplementary Fig. 13). Moreover, A-Ni@CS affords low charge transfer resistance and fast activation kinetics, as confirmed by electrochemical impedance spectroscopy (Fig. 2f; Supplementary Fig. 14). The Tafel slope of A-Ni@CS showed 161 mV/dec for CO_2 reduction (Fig. 2g), which is closed to 120 mv/dec, demonstrating the first electron transfer ($CO_2 \rightarrow COOH^*$) is the rate-determining step [20,37,38]. A-Ni@CS was extremely stable during CO production, maintaining a high FE_{CO} (90.5 %) even after 80 h of continuous operation (Fig. 2h). The decreased in the performance of A-Ni@CS is possibly because of the mechanical shedding of the catalysts and the formation of K-based salts on the catalyst surface (Supplementary Fig. 15), thereby destroying the active sites.

The H-cells show a limited current density of < 50 mA/cm^2 because of the slow diffusion and low solubility of CO_2 in aqueous electrolytes.[7] This issue can be resolved by employing a zero-gap flow cell with a GDE (Fig. 3a; Supplementary Fig. 16). A-Ni@CS exhibits a high selectivity of near-unity for CO at various current densities and reaches the highest value at 150 mA/cm^2 (FE_{CO}=99.4 %) (Fig. 3b; Supplementary Table S2). Besides, A-Ni@CS shows a 2.2 V full-cell voltage (E_{cell}) at 200 mA/cm^2, which is 0.3 V lower than that of A-Ni@CB under the same condition (2.5 V). Compared to recently developed state-of-the-art catalysts (Fig. 3c; Supplementary Table S1–S2), A-Ni@CS exhibits an outstanding selectivity and a higher current density (FE_{CO}=98.55 %, 200 mA/cm^2), which greatly increases the rate of CO production. More importantly, Fig. 3d shows that A-Ni@CS delivers a significant full-cell EE>60 % at

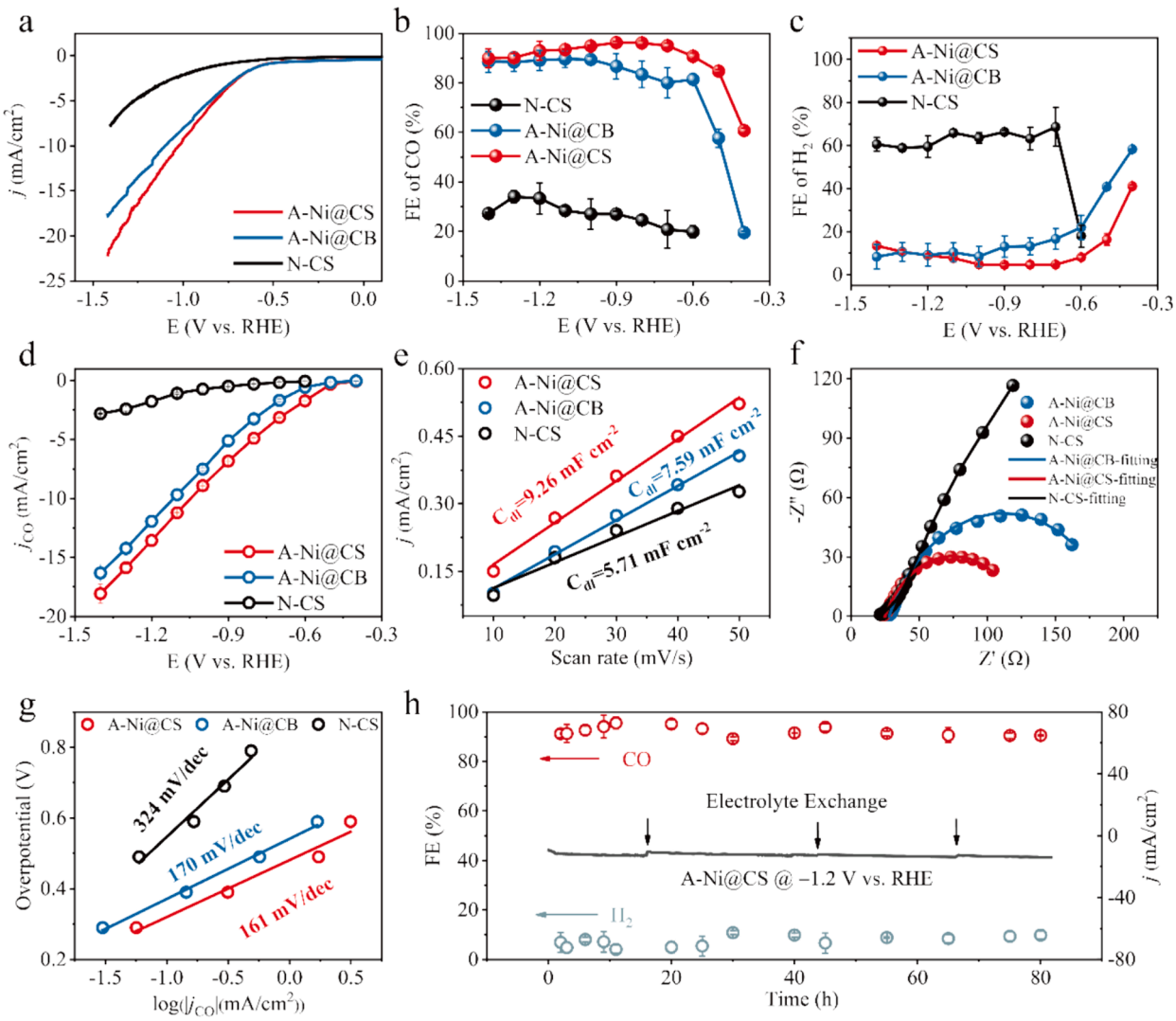

Fig.2. Electrochemical CO_2RR performance of A-Ni@CS, A-Ni@CB, and N-CS in a conventional H-cell. (a) LSV curves in CO_2-saturated $KHCO_3$ (0.1 M) at a scan rate of 20 mV/s. (b) FE of CO and (c) H_2 at various potentials. (d) CO partial current densities. (e) Double layer capacitance. (f) Nyquist plots (Electrochemical impedance spectroscopy (EIS) was measured at frequencies ranging from 10 MHz to 100 mHz at − 0.5 V vs. RHE). (g) Tafel slopes. (h) Long-term stability test of A-Ni@CS for 80 h at − 1.2 V vs. RHE.

various current densities. Even at an industrially relevant current density (200 mA/cm^2), A-Ni@CS also possesses a 60 % EE, to our knowledge, achieving the highest full-cell EE under the same condition reported so far. Specifically, the EE (Supplementary Table S2) increases by ~ 10 % under the same current density, compared to that of recently developed state-of-the-art Ni SACs (EE: 51 %, 125 mA/cm^2) and CoPc (EE: 47 %, 200 mA/cm^2) electrocatalysts. In contrast to the noble Ag-metal electrocatalysts (EE: 44 %), the EE of A-Ni@CS increased by 16 % when 200 mA/cm^2 was applied.

Fig. 3f and Supplementary Fig. 13 exhibit that A-Ni@CS with a loading of 1 mg/cm^2 has the best activity for the CO_2RR owing to its suitable active sites number and CO_2 transport. Fig. 3g shows that the activity of CO_2RR decreases and the activity of the HER increases for both A-Ni@CS and A-Ni@CB as the CO_2 flow rate decreases. When the CO_2 flow rate is 5 sccm, the FE_{CO} of A-Ni@CS is 57.8 %, much higher than that of A-Ni@CB (1.7 %). Fig. 3h shows that FE_{CO} decreases and the FE of H_2 increases with the decrease of the partial pressure of CO_2. When the partial pressure of CO_2 is 0.15 bar, the FE_{CO} of A-Ni@CS and A-Ni@CB are 49.5 % and 3.7 %, respectively. This variation confirms that low local CO_2 concentration results in a poor performance of the CO_2RR, and this issue becomes more severe with the increase of current densities. Additionally, this difference probably demonstrates that the macroporous structure and the large porosity of A-Ni@CS can facilitate the local CO_2 transport and improve the local CO_2 concentration in the CL. A-Ni@CS exhibited a FE_{CO} of 93.8 % after 6 h continuous operation in the 1 M KOH media (Supplementary Fig. 12a). The slight decrease in the performance is probably attributed to water flooding [39–41] and (bi)carbonate salt formation [42], which destroy the triple-phase interface. To alleviate this problem, we evaluated the catalytic performance in a neutral electrolyte solution (*i.e.*, 0.1 M $KHCO_3$) (Supplementary Fig. 17). Fig. 3i exhibits that A-Ni@CS maintains a high FE_{CO} nearly 90 % during the continuous operation, and achieves an 88.7 % FE_{CO} after 20 h electrolysis. Besides, post-electrolysis characterization of A-Ni@CS confirmed the catalyst maintained the initial macroporous structure (Supplementary Fig. 18).

3.3. Electronic structure and coordination environment analysis.

X-ray characterization studies were conducted to understand the enhanced intrinsic activity of A-Ni@CS for the CO_2RR. The high-resolution N 1 s XPS spectrum of A-Ni@CS (Fig. 4a) can be divided into five subpeaks: pyridinic N (398.5 eV), Ni–N (399.1 eV), pyrrolic N

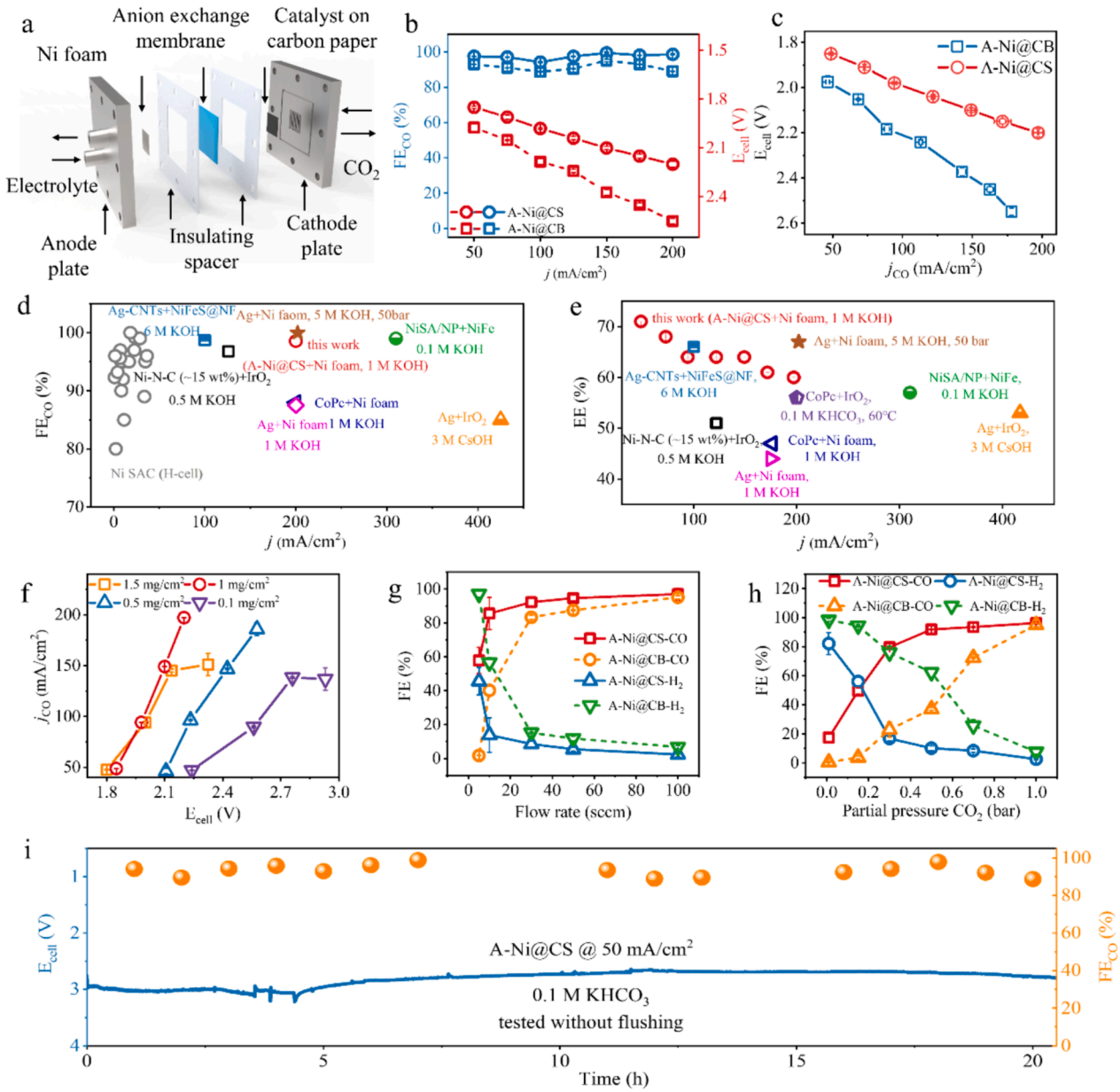

Fig.3. Electrochemical CO_2RR performance in a zero-gap flow cell. (a) Schematic of a zero-gap flow cell. (b) Electrochemical CO_2RR performance of A-Ni@CS and A-Ni@CB in a zero-gap flow cell: E_{cell} and FE_{CO} at various current densities. (c) The corresponding j_{CO} of A-Ni@CS and A-Ni@CB catalyst at different applied voltages. (d–e) CO_2RR performance of A-Ni@CS (2.1 wt%, this work, red) and recently developed state-of-the-art catalysts (Ag (brown) [43], CoPc (blue) [5], Ni SAC (15 wt%, black) [44], Ag (orange) [45], Ag-CNTs (blue) [46], NiSA/NP (green) [47], CoPc (purple) [48], and other Ni SAC in the H-cell (gray, details in Table S1)). (f) The corresponding j_{CO} of A-Ni@CS catalyst with different loadings at various applied voltages. The corresponding FE of A-Ni@CS and A-Ni@CB catalyst (1 mg/cm^2) at (g) various CO_2 flow rate and (h) different CO_2 partial pressure. (i) The long-term stability of A-Ni@CS catalyst (1 mg/cm^2) at 50 mA/cm^2 using 0.1 M $KHCO_3$ electrolyte solution. (For interpretation of the references to color in this figure legend, the reader is referred to the web version of this article.)

(400.5 eV), quaternary N (401.9 eV), and oxidized N (404.9 eV). Among these different N species for A-Ni@CS (Supplementary Fig. 10d), Ni–N was present in the largest amount, which confirms the presence of abundant intrinsic active sites. The O 1 s XPS spectrum of A-Ni@CS shows distinct Ni-O species at 531.4 eV (Fig. 4b). In contrast, the largest amount of N species was pyridinic N, and no distinct Ni–O bonds were detected over A-Ni@CB (Supplementary Fig. 10 h–j).

To explore the coordination environment of the atomic Ni sites, XAS of A-Ni@CS and A-Ni@CB was performed. We selected Ni foil, NiO, and nickel phthalocyanine (NiPc) as references. The pre-edge features of A-Ni@CB are close to those of NiPc, but they are different from those of A-Ni@CS. NiPc exhibits a distinct fingerprint of Ni 1 s to the $4p_z$ orbital at ~ 8340 eV (Fig. 4c). The fingerprint is not obvious in either A-Ni@CS or A-Ni@CB, which confirms that their structures are different from those of typical Ni–N_4 models. A-Ni@CS and A-Ni@CB display distinct characteristic peaks at 1.61 and 1.33 Å, respectively. No obvious Ni–Ni scattering path was observed at 2.19 Å, demonstrating the presence of atomic Ni species (Fig. 4d). The characteristic peaks of NiO and NiPc are located at 2.60 (Ni–O) and 1.48 Å (Ni–N), respectively. The wavelet transform (WT) maximum of A-Ni@CS was observed at 4.7 Å^{-1}, close to that of A-Ni@CB (~5 Å^{-1}), but considerably different from those of Ni foil, NiO, and NiPc (Supplementary Fig. 17). Moreover, the WT maximum corresponding to Ni–Ni bonds was not observed in either A-Ni@CS or A-Ni@CB, confirming the presence of atomically dispersed Ni species. Furthermore, EXAFS fitting curves of A-Ni@CS and A-Ni@CB in R space were conducted to obtain the quantitative structural parameters

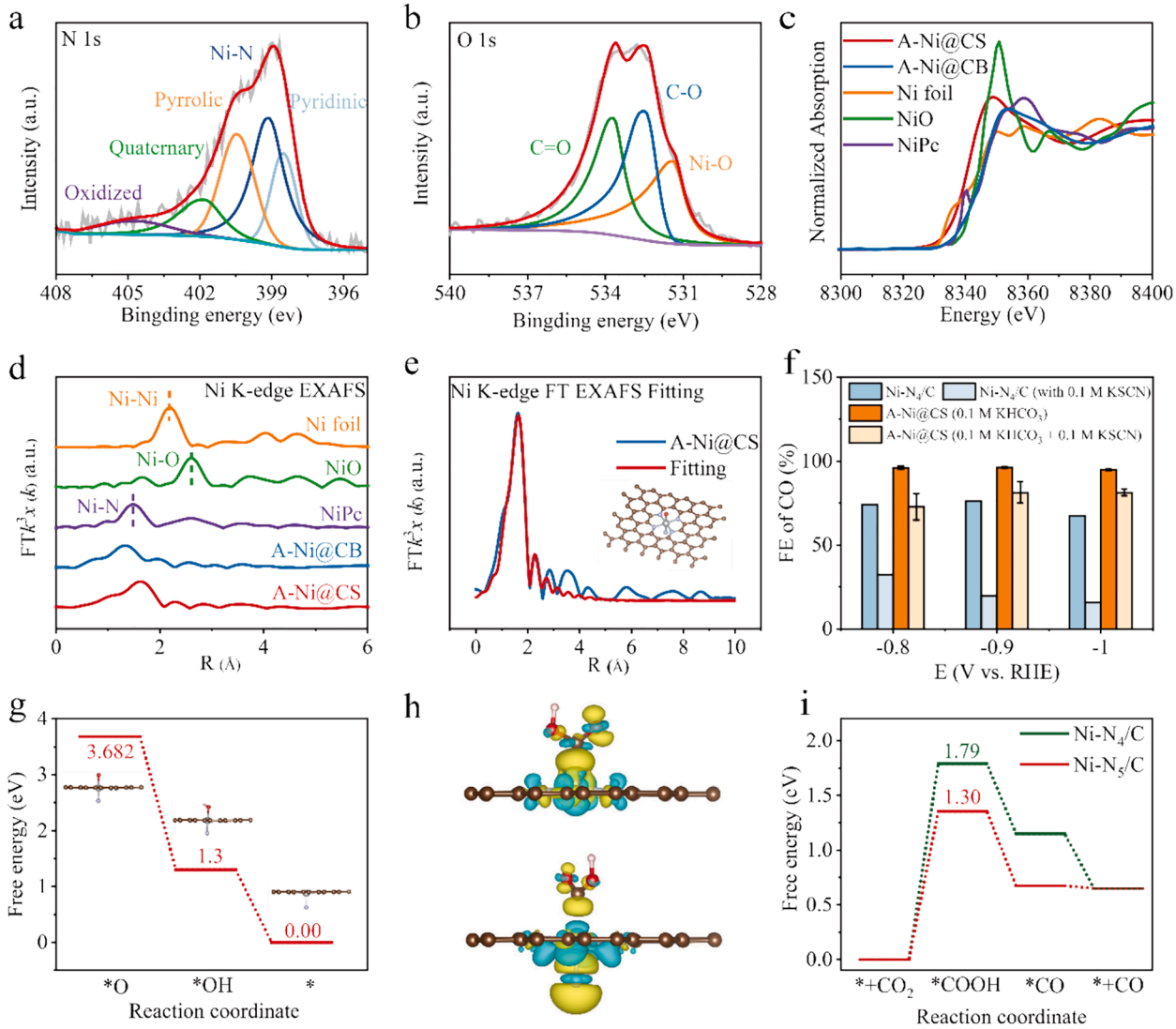

Fig.4. Coordination Environment Analysis. High-resolution (a) N 1 s and (b) O 1 s XPS spectra of A-Ni@CS. (c) Ni K-edge X-ray absorption near–edge structure (XANES) spectra and (d) Ni K-edge Fourier-transformed extended X-ray absorption fine structure (EXAFS) spectra of A-Ni@CS, A-Ni@CB, Ni foil, NiO, and NiPc. (e) EXAFS fitting curve of A-Ni@CS in R space. (f) FE_{CO} of A-Ni@CS (orange) and Ni–N_4/C (blue)[11] before and after poisoning. (g) Possible mechanism of Gibbs free energy profiles for electroreduction from Ni − N_5 − O/C to Ni − N_5/C. (h) Difference of electron density for *COOH intermediates absorbed on Ni–N_4/C and Ni–N_5/C. (i) Reaction paths and free energy diagrams of CO_2 reduction to CO over Ni–N_4/C and Ni–N_5/C catalytic sites. (For interpretation of the references to color in this figure legend, the reader is referred to the web version of this article.)

around central Ni atoms (Fig. 4e; Supplementary Fig. 17 and Table 3). It can be speculated that the atomic Ni sites of A-Ni@CS and A-Ni@CB have the Ni–N_5–O/C and Ni–N_5/C coordination environments.

Thiocyanate ion (SCN^-) poisoning tests were conducted to determine the reaction mechanisms and intrinsic active sites of A-Ni@CS. KSCN was added as an inhibitor to the electrolyte to block and destroy the Ni–N_4 sites. A-Ni@CS still exhibits significantly high FE_{CO} after SCN^- poisoning (*e.g.*, −0.8 V vs. RHE, FE_{CO}=72.7 %), which can be explained by the axial atom traction in A-Ni@CS that protects the active sites from being poisoned (Fig. 4f). In contrast, the FE_{CO} of the Ni–N_4/C catalysts sharply declined after SCN^- poisoning.

DFT calculations were performed to further understand the intrinsic reactivity and property. Fig. 4g shows that an axial absorbed O atom is active to interact with protons and desorb into the electrolyte during CO_2 electrolysis, which is also confirmed by the post-electrolysis characterization (*i.e.*, XPS) of A-Ni@CS (Supplementary Fig. 10), suggesting the real active sites of A-Ni@CS for the CO_2RR are probably attributed to Ni–N_5/C. Thus, two typical structures (Ni–N_4/C and Ni–N_5/C) were employed as models for the following calculations (Supplementary Fig. 18). The reaction pathways for the electrochemical conversion of CO_2 to CO include four steps (Supplementary Fig. 18), in which the formation of *COOH is always regarded as the rate-limiting step [49]. Fig. 4h illustrates that the axial traction of a nitrogen atom leads to more significant charge polarization on Ni–N_5/C active sites than on Ni–N_4/C active sites. The energy barrier of *COOH formation is reduced on the dynamic activation of Ni–N_5/C active sites for the CO_2RR compared to that of Ni–N_4/C active sites. Fig. 4i shows that Ni–N_4/C and Ni–N_5/C deliver 1.79 and 1.30 eV of free energies for the formation of *COOH, respectively, confirming that Ni–N_5/C has a surprisingly lower energy barrier for the CO_2RR, consistent with the abovementioned experimental studies.

3.4. Tomographic reconstruction and pore-network modeling.

Apart from the enhanced intrinsic activity of the prepared catalysts, the mass transfer and concentration of reactants in the CL significantly contributes to the final performance, especially at industrial current densities [23]. The optimization of the pore size structure and

distribution in CLs has critical effects on the reactant transport and local CO_2 concentration, but is always neglected. Thus, we studied the effects of the CL porous structure and morphology on the CO_2RR, which would fundamentally determine the D_{eff}/D_0 of the reactants and their local concentrations. Both A-Ni@CS and A-Ni@CB have large pores (10 s of microns, cracks) and nano-scale pores, indicating multiscale pore structures (Supplementary Video 1–2). These large pores are probably formed due to the uneven heating during the catalyst spraying process. These large cracks and nano-scale pores in the CL could provide transport channels for H_2O and CO_2, respectively [50,51]. Besides, the large pores in A-Ni@CS and A-Ni@CB are similar and close in size. The main distinction between A-Ni@CS and A-Ni@CB is in the nanoscale pore region. Thus, a detailed comparison was conducted specifically focusing on the nano-scale pores portion.

Tomographic reconstruction of the CL was conducted through focused ion beam scanning electron microscopy (FIB-SEM). Fig. 5a and Supplementary Fig. 21 show the reconstructions of the A-Ni@CS and A-Ni@CB CLs. The A-Ni@CS CL possesses a porosity of 75 %, which is higher than those of the A-Ni@CB CL (porosity: 35 %) and other reported CLs in polymer electrolyte fuel cells (porosity: ~50 %) [52] and polymer electrolyte water electrolyzers (porosity: ~53 %) [53]. The mean porosity and pore size distribution of the A-Ni@CS CL in the x-direction were spatially resolved (Fig. 5b–c). Both the A-Ni@CS and A-Ni@CB CLs exhibited uniform porosity and pore size distributions along the three main directions (x, y, and z). A mean pore size of ~ 122 nm was observed for the A-Ni@CS CL, which is almost double that of the A-Ni@CB CL (~65 nm). The pore size distribution of A-Ni@CS and A-Ni@CB CL shows that the pore size on average of A-Ni@CS CL are larger than those of A-Ni@CB CL (Supplementary Fig. 22). These macropores could facilitate the local CO_2 mass transfer and increase the CO_2 concentration in the CL, while the mesopores on the walls improved the specific surface area. The layered nano-to-micro porous structure synergistically enhanced the electrochemical activity of the CO_2RR.

In the cathodic CL, for every mole of CO_2, one mole of CO is produced, while the partial pressure of water remains steady. Although different Knudsen diffusion coefficients may introduce a small pressure gradient, the convection is negligible. Thus, the main mechanism of CO_2 transport in the CL during the CO_2RR is assumed to be diffusion. To assess the local reactant mass transfer in the CLs, we employed the PNM to conduct a quasi-static analysis of the two-phase flow in the CLs based on the reconstructed porous structures. Gas and liquid distributions under different gas-phase saturations (S_w, corresponding to water flooding in the CL during CO_2 electrolysis) were obtained (Fig. 5d; Supplementary Fig. 21f). As the electrolyzer operates, an increasing amount of water floods the pore spaces of the CL. We plotted the D_{eff}/D_0 of the solute in the liquid and CO_2 in the gaseous mixture versus S_w. The D_{eff}/D_0 of CO_2 for both samples decrease with the decrease in S_w because of water flooding. However, the A-Ni@CS CL delivered 6.7 times larger D_{eff}/D_0 for CO_2 (0.1) than that of the A-Ni@CB CL (0.028) when 0.5 S_w was applied. The increased D_{eff}/D_0 for the A-Ni@CS CL was attributed to its high porosity and excellent pore connectivity (confirmed by the coordination numbers of pores, as shown in Supplementary Fig. 21i). In addition, the enhanced Knudsen effects in the A-Ni@CB CL increased the diffusion resistance of CO_2, which further decreased D_{eff}/D_0 for the A-Ni@CS CL. The larger coordination numbers and high porosity of the A-Ni@CS CL provide numerous less-resistant transport pathways for the reactants, which can increase the local CO_2 concentration in the CL and enhance the final performance of the CO_2RR.

Additionally, other phenomena, such as pore blockage due to water or salt accumulation, also have important effects on the local reactant concentration and electrochemical performance. However, it is challenging to quantify the saturation under real conditions. The PNM

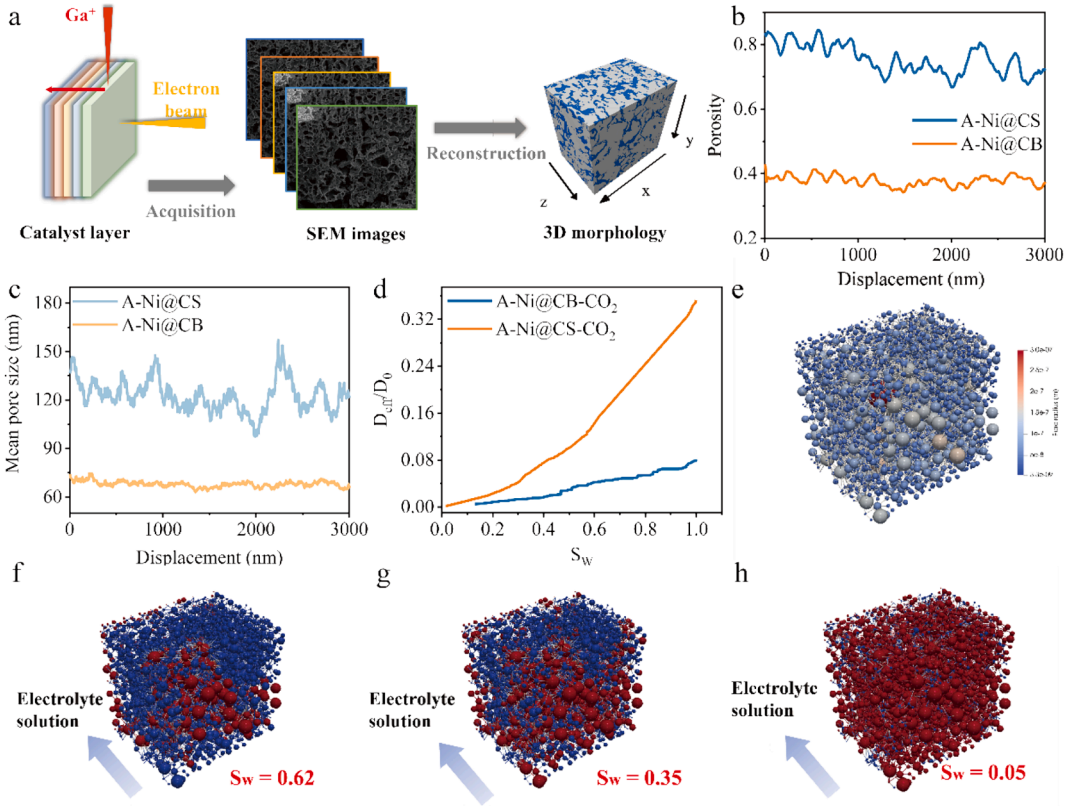

Fig.5. Local CO_2 transport in the CLs. (a) Reconstructed porous structures of A-Ni@CS by FIB-SEM (pore space is in gray, solid is blue). Mean porosity (b) and mean diameter (c) of inscribed circles distributed along the x-direction. (d) Relationship between D_{eff}/D_0 of CO_2 with different S_w. (e) The extracted pore network of A-Ni@CS CL. (f-h) Gas-liquid distributions in A-Ni@CS at different S_w values. (S_w, wetting saturation of gaseous mixture; color scheme: red, liquid; blue, gas). (For interpretation of the references to color in this figure legend, the reader is referred to the web version of this article.)

results show that the D_{eff}/D_0 of CO_2 for A-Ni@CS is larger than that for A-Ni@CB under the same saturation. Although A-Ni@CS may have a lower S_w than that of the A-Ni@CB under real conditions, A-Ni@CS still shows a larger D_{eff}/D_0 of CO_2 than that of the A-Ni@CB. For example, the D_{eff}/D_0 of CO_2 for A-Ni@CB is 0.028 when the S_w is 0.5. The D_{eff}/D_0 of CO_2 for A-Ni@CS is 0.042 when the S_w is 0.3. Pore blockage due to water or salt accumulation and CO_2 transport together determine the final performance.

Furthermore, we recorded the start-up curves of A-Ni@CS and A-Ni@CB in the zero-gap flow cell. The humidified CO_2 was used as the reactant and transported to the cathode at least 10 min before tests. The flow rate of CO_2 was set as 100 sccm. As shown in Supplementary Fig. 23, when time begins at 0 s, the electrolyzer starts with a constant current density of − 200 mA/cm^2. The variation of E_{cell} of A-Ni@CS and A-Ni@CB along with time were then detected. The initial fluctuations reflected the process of forming a triple-phase interface because the GDE was dry before use. A-Ni@CS exhibits a shorter start-up time than that of A-Ni@CB, demonstrating that the former can facilitate rapid transport of reactants (CO_2 and water) and can more easily form a stable triple-phase interface. Overall, combined with interconnected macropores of CS which significantly increase the local concentration of CO_2 in the CL and the superior intrinsic activity of A-Ni@CS, we get the highest EE of 60 % at an industrial current density (200 mA/cm^2), which provide a unique insight to drive industrial applications of CO_2 electrolysis.

4. Conclusions

We presented a Ni–N_5–O/C single-atom catalyst anchored on CS and demonstrated that tuning the coordination structure of Ni metal centers enables the intrinsic activity of the CO_2RR. HRTEM images, X-ray measurements, and poisoning tests confirmed the occurrence of atomically dispersed Ni and its unique Ni–N_5–O/C structure. DFT analysis demonstrated that an optimized coordination environment can lower the energy barrier of intermediate *COOH formation and improve the intrinsic activity of the CO_2RR. Tomographic reconstruction of the CL indicated that A-Ni@CS possessed a large porosity (75 %), abundant macroporous structure (~122 nm), and high connectivity of pore spaces. Furthermore, PNM analysis confirmed that the D_{eff} of CO_2 in the A-Ni@CS CL was extremely enhanced, significantly increasing the local CO_2 concentration. A-Ni@CS exhibited a high FE_{CO} (98.5 %) and excellent full-cell EE (60 %) at the industrially relevant current density (200 mA/cm^2) for mediating CO_2 to CO in a zero-gap flow cell. Apart from the optimization of the intrinsic activity, the CL design strategy in this study not only highlights the importance of reactant transport but also offers a unique insight into the development of the CO_2RR. Future studies should focus on *in situ* technologies and numerical calculations at the nanoscale to detect the local reactant transport during the CO_2RR, especially when the products are complex.

CRediT authorship contribution statement

Pengtao Yue: Writing – review & editing, Writing – original draft, Visualization, Methodology, Investigation, Funding acquisition, Formal analysis, Data curation, Conceptualization. **Junjun Wu:** Writing – review & editing, Software, Project administration, Investigation, Data curation, Conceptualization. **Chaozhong Qin:** Writing – review & editing, Software, Project administration, Methodology, Formal analysis, Data curation, Conceptualization. **Bowen Shi:** Writing – review & editing, Software, Formal analysis, Data curation, Conceptualization. **Yang Wang:** Writing – review & editing, Software, Methodology, Investigation, Data curation. **Yue Zhang:** Writing – review & editing, Methodology, Investigation, Formal analysis, Data curation. **Yanan Zou:** Writing – review & editing, Software, Methodology, Investigation, Data curation. **Jun Li:** Writing – review & editing, Visualization, Project administration, Formal analysis, Data curation. **Liang Zhang:** Writing – review & editing, Investigation, Funding acquisition, Formal analysis, Conceptualization. **Xun Zhu:** Writing – review & editing, Investigation, Data curation, Conceptualization. **Miao Zhong:** Writing – review & editing, Software, Formal analysis, Data curation. **Qian Fu:** Writing – review & editing, Validation, Supervision, Project administration, Methodology, Investigation, Funding acquisition, Formal analysis, Data curation, Conceptualization. **Qiang Liao:** Writing – review & editing, Project administration, Methodology, Investigation, Funding acquisition, Formal analysis, Data curation, Conceptualization.

Declaration of competing interest

The authors declare that they have no known competing financial interests or personal relationships that could have appeared to influence the work reported in this paper.

Data availability

Data will be made available on request.

Acknowledgements

This work was supported by the National Natural and Science Foundation of China (No. 52076021, 52021004), Natural Science Funds for Distinguished Young Scholar of Chongqing, China (No. cstc2019jcyjjqX0020), Fundamental Research Funds for the Central Universities (No. 2021CDJQY-045, 2023CDJXY-012), and Graduate Student Research Innovation Project of Chongqing, China (No. CYB21022).

Appendix A. Supplementary data

Supplementary data to this article can be found online at https://doi.org/10.1016/j.cej.2024.154607.

References

[1] R. Boppella, Y. Kim, K.A. Joshi Reddy, I. Song, Y. Eom, E. Sim, T.K. Kim, Synergistic electronic structure modulation in single-atomic Ni sites dispersed on Ni nanoparticles encapsulated in N-rich carbon nanotubes synthesized at low temperature for efficient CO_2 electrolysis, Appl. Catal. B Environ. 345 (2024) 123699–123710.

[2] Z. Liu, T. Yan, H. Shi, H. Pan, P. Kang, Grafting amine-functionalized ligand layer on catalyst for electrochemical CO_2 capture and utilization, Appl. Catal. B Environ. 343 (2024) 123456–123464.

[3] X. Sun, L. Wang, X. Lan, Q. Lu, Y. Tuo, C. Ye, D. Wang, C. Xu, Positively charged nickel-sulfur dual sites for efficient CO_2 electroreduction reaction, Appl. Catal. B Environ. 342 (2024) 123389–123396.

[4] S. Van Daele, L. Hintjens, S. Hoekx, B. Bohlen, S. Neukermans, N. Daems, J. Hereijgers, T. Breugelmans, How flue gas impurities affect the electrochemical reduction of CO_2 to CO and formate, Appl. Catal. B Environ. 341 (2024) 123345–123354.

[5] S. Ren, D. Joulie, D. Salvatore, K. Torbensen, M. Wang, M. Robert, C. P. Berlinguette, Molecular electrocatalysts can mediate fast, selective CO_2 reduction in a flow cell, Science 365 (2019) 367–369.

[6] T.T. Zheng, K. Jiang, N. Ta, Y.F. Hu, J. Zeng, J.Y. Liu, H.T. Wang, Large-scale and highly selective CO_2 electrocatalytic reduction on nickel single-atom catalyst, Joule 3 (2019) 265–278.

[7] B. Siritanaratkul, M. Forster, F. Greenwell, P.K. Sharma, E.H. Yu, A.J. Cowan, Zero-gap bipolar membrane electrolyzer for carbon dioxide reduction using acid-tolerant molecular electrocatalysts, J. Am. Chem. Soc. 144 (2022) 7551–7556.

[8] C. Ding, C. Feng, Y. Mei, F. Liu, H. Wang, M. Dupuis, C. Li, Carbon nitride embedded with transition metals for selective electrocatalytic CO_2 reduction, Appl. Catal. B Environ. 268 (2020) 118391–118398.

[9] G. Hyun, J.T. Song, C. Ahn, Y. Ham, D. Cho, J. Oh, S. Jeon, Hierarchically porous Au nanostructures with interconnected channels for efficient mass transport in electrocatalytic CO_2 reduction, Proc. Natl. Acad. Sci. 117 (2020) 5680–5685.

[10] A. Reyes, R.P. Jansonius, B.A.W. Mowbray, Y. Cao, D.G. Wheeler, J. Chau, D. J. Dvorak, C.P. Berlinguette, Managing hydration at the cathode enables efficient CO_2 electrolysis at commercially relevant current densities, Acs Energy Lett. 5 (2020) 1612–1618.

[11] M. Huang, B. Deng, X. Zhao, Z. Zhang, F. Li, K. Li, Z. Cui, L. Kong, J. Lu, F. Dong, L. Zhang, P. Chen, Template-sacrificing synthesis of well-defined asymmetrically coordinated single-atom catalysts for highly efficient CO_2 electrocatalytic reduction, ACS Nano 16 (2022) 2110–2119.

[12] P. De Luna, C. Hahn, D. Higgins, S.A. Jaffer, T.F. Jaramillo, E.H. Sargent, What would it take for renewably powered electrosynthesis to displace petrochemical processes? Science 364 (2019) 350–358.

[13] R.I. Masel, Z. Liu, H. Yang, J.J. Kaczur, D. Carrillo, S. Ren, D. Salvatore, C. P. Berlinguette, An industrial perspective on catalysts for low-temperature CO_2 electrolysis, Nat. Nanotechnol. 16 (2021) 118–128.

[14] D.I. Tishkevich, A.I. Vorobjova, D.L. Shimanovich, D.A. Vinnik, T.I. Zubar, A. L. Kozlovskiy, M.V. Zdorovets, D.V. Yakimchuk, S.V. Trukhanov, A.V. Trukhanov, Formation and corrosion properties of Ni-based composite material in the anodic alumina porous matrix, J. Alloy. Compd. 804 (2019) 139–146.

[15] A. Kotelnikova, T. Zubar, T. Vershinina, M. Panasyuk, O. Kanafyev, V. Fedkin, I. Kubasov, A. Turutin, S. Trukhanov, D. Tishkevich, V. Fedosyuk, A. Trukhanov, The influence of saccharin adsorption on NiFe alloy film growth mechanisms during electrodeposition, RSC Adv 12 (2022) 35722–35729.

[16] Y. Li, S.L. Zhang, W. Cheng, D. Luan, S. Gao, X.W.D. Lou, Loading single-Ni atoms on assembled hollow N-rich carbon plates for efficient CO_2 electroreduction, Adv. Mater. 2105204–2105211 (2021).

[17] S. Liang, Q. Jiang, Q. Wang, Y. Liu, Revealing the real role of nickel decorated nitrogen-doped carbon catalysts for electrochemical reduction of CO_2 to CO, Adv. Energy Mater. 11 (2021) 2101477–2101490.

[18] X. Wang, Y. Wang, X. Sang, W. Zheng, S. Zhang, L. Shuai, B. Yang, Z. Li, J. Chen, L. Lei, N.M. Adli, M.K.H. Leung, M. Qiu, G. Wu, Y. Hou, Dynamic activation of adsorbed intermediates via axial traction for the promoted electrochemical CO_2 reduction, Angew. Chem. Int. Ed. Engl. 60 (2021) 4192–4198.

[19] Y. Zhang, K. Qi, J. Li, B.A. Karamoko, L. Lajaunie, F. Godiard, E. Oliviero, X. Cui, Y. Wang, Y. Zhang, H. Wu, W. Wang, D. Voiry, 2.6% cm^{-2} single-pass CO_2-to-CO conversion using Ni single atoms supported on ultra-thin carbon nanosheets in a flow electrolyzer, ACS Catal. 11 (2021) 12701–12711.

[20] X. Zhao, S. Huang, Z. Chen, C. Lu, S. Han, C. Ke, J. Zhu, J. Zhang, D. Tranca, X. Zhuang, Carbon nanosheets supporting Ni–N_3S single-atom sites for efficient electrocatalytic CO_2 reduction, Carbon 178 (2021) 488–496.

[21] D. Wakerley, S. Lamaison, F. Ozanam, N. Menguy, D. Mercier, P. Marcus, M. Fontecave, V. Mougel, Bio-inspired hydrophobicity promotes CO_2 reduction on a Cu surface, Nat. Mater. 18 (2019) 1222–1227.

[22] H. Rabiee, L. Ge, X. Zhang, S. Hu, M. Li, Z. Yuan, Gas diffusion electrodes (GDEs) for electrochemical reduction of carbon dioxide, carbon monoxide, and dinitrogen to value-added products: a review, Energy Environ. Sci. 14 (2021) 1959–2008.

[23] F.P.G. de Arquer, C.T. Dinh, A. Ozden, J. Wicks, C. McCallum, A.R. Kirmani, D. H. Nam, C. Gabardo, A. Seifitokaldani, X. Wang, Y.G.C. Li, F.W. Li, J. Edwards, L. J. Richter, S.J. Thorpe, D. Sinton, E.H. Sargent, CO_2 electrolysis to multicarbon products at activities greater than 1 A cm^{-2}, Science 367 (2020) 661–667.

[24] Y. Pan, R. Lin, Y. Chen, S. Liu, W. Zhu, X. Cao, W. Chen, K. Wu, W.C. Cheong, Y. Wang, L. Zheng, J. Luo, Y. Lin, Y. Liu, C. Liu, J. Li, Q. Lu, X. Chen, D. Wang, Q. Peng, C. Chen, Y. Li, Design of single-atom Co-N_5 catalytic site: a robust electrocatalyst for CO_2 reduction with nearly 100% CO selectivity and remarkable stability, J. Am. Chem. Soc. 140 (2018) 4218–4221.

[25] H.B. Yang, S.-F. Hung, S. Liu, K. Yuan, S. Miao, L. Zhang, X. Huang, H.-Y. Wang, W. Cai, R. Chen, J. Gao, X. Yang, W. Chen, Y. Huang, H.M. Chen, C.M. Li, T. Zhang, B. Liu, Atomically dispersed Ni(i) as the active site for electrochemical CO_2 reduction, Nat. Energy 3 (2018) 140–147.

[26] E. Nagy, Membrane Gas Separation, Basic Equations of Mass Transport through a Membrane Layer (2019) 457–481.

[27] A.V. Trukhanov, D.I. Tishkevich, S.V. Podgornaya, E. Kaniukov, M.A. Darwish, T. I. Zubar, A.V. Timofeev, E.L. Trukhanova, V.G. Kostishin, S.V. Trukhanov, Impact of the Nanocarbon on Magnetic and Electrodynamic Properties of the Ferrite/ Polymer Composites, Nanomaterials (basel) 12 (2022).

[28] G. Kresse, J. Furthmuller, Efficient iterative schemes for ab initio total-energy calculations using a plane-wave basis set, Phys. Rev. B 54 (1996) 11169–11186.

[29] P.E. Blochl, Projector augmented-wave method, Physical Review B 50 (1994) 17953–17979.

[30] J.P. Perdew, M. Kieron Burke, Ernzerhof,, Generalized gradient approximation made simple, Phys. Rev. Lett. 77 (1996) 3865–3868.

[31] S.L. Dudarev, G.A. Botton, S.Y. Savrasov, C.J. Humphreys, A.P. Sutton, Electron-energy-loss spectra and the structural stability of nickel oxide: An LSDA+U study, Phys. Rev. B 57 (1998) 1505–1509.

[32] S. Grimme, J. Antony, S. Ehrlich, H. Krieg, A consistent and accurate ab initio parametrization of density functional dispersion correction (DFT-D) for the 94 elements H-Pu, J. Chem. Phys. 132 (2010) 154104.

[33] S. Grimme, S. Ehrlich, L. Goerigk, Effect of the damping function in dispersion corrected density functional theory, J. Comput. Chem. 32 (2011) 1456–1465.

[34] J.T. Gostick, Versatile and efficient pore network extraction method using marker-based watershed segmentation, Phys. Rev. E 96 (2017) 023307.

[35] C.-Z. Qin, H. van Brummelen, M. Hefny, J. Zhao, Image-based modeling of spontaneous imbibition in porous media by a dynamic pore network model, Adv. Water Resources 152 (2021) 103932–103944.

[36] M. Hefny, C. Qin, M.O. Saar, A. Ebigbo, Synchrotron-based pore-network modeling of two-phase flow in Nubian Sandstone and implications for capillary trapping of carbon dioxide, Int. J. Greenh. Gas Con. 103 (2020) 103164.

[37] W. Ren, X. Tan, X. Chen, G. Zhang, K. Zhao, W. Yang, C. Jia, Y. Zhao, S.C. Smith, C. Zhao, Confinement of ionic liquids at single-Ni-sites boost electroreduction of CO_2 in aqueous electrolytes, ACS Catal. 10 (2020) 13171–13178.

[38] M. Gattrell, N. Gupta, A. Co, A review of the aqueous electrochemical reduction of CO_2 to hydrocarbons at copper, J. Electroanal. Chem. 594 (2006) 1–19.

[39] J. Disch, L. Bohn, S. Koch, M. Schulz, Y. Han, A. Tengattini, L. Helfen, M. Breitwieser, S. Vierrath, High-resolution neutron imaging of salt precipitation and water transport in zero-gap CO_2 electrolysis, Nat. Commun. 13 (2022) 6099–6107.

[40] L. Li, J. Chen, V.S.S. Mosali, Y. Liang, A.M. Bond, Q. Gu, J. Zhang, Hydrophobicity graded gas diffusion layer for stable electrochemical reduction of CO_2, Angew. Chem. Int. Ed. Engl. (2022) e202208534.

[41] Y. Wu, L. Charlesworth, I. Maglaya, M.N. Idros, M. Li, T. Burdyny, G. Wang, T. E. Rufford, Mitigating electrolyte flooding for electrochemical CO_2 reduction via infiltration of hydrophobic particles in a gas diffusion layer, ACS Energy Lett. 7 (2022) 2884–2892.

[42] A. Ozden, F.P. García de Arquer, J.E. Huang, J. Wicks, J. Sisler, R.K. Miao, C. P. O'Brien, G. Lee, X. Wang, A.H. Ip, E.H. Sargent, D. Sinton, Carbon-efficient carbon dioxide electrolysers, Nat. Sustain. 5 (2022) 563–573.

[43] J.P. Edwards, Y. Xu, C.M. Gabardo, C.-T. Dinh, J. Li, Z. Qi, A. Ozden, E.H. Sargent, D. Sinton, Efficient electrocatalytic conversion of carbon dioxide in a low-resistance pressurized alkaline electrolyzer, Appl. Energy 261 (2020) 114305–114311.

[44] C. Xia, Y. Qiu, Y. Xia, P. Zhu, G. King, X. Zhang, Z. Wu, J.Y.T. Kim, D.A. Cullen, D. Zheng, P. Li, M. Shakouri, E. Heredia, P. Cui, H.N. Alshareef, Y. Hu, H. Wang, General synthesis of single-atom catalysts with high metal loading using graphene quantum dots, Nat. Chem. 13 (2021) 887–894.

[45] S.S. Bhargava, F. Proietto, D. Azmoodeh, E.R. Cofell, D.A. Henckel, S. Verma, C. J. Brooks, A.A. Gewirth, P.J.A. Kenis, System design rules for intensifying the electrochemical reduction of CO_2 to CO on Ag nanoparticles, ChemElectroChem 7 (2020) 2001–2011.

[46] S. Li, Y. Ma, T. Zhao, J. Li, X. Kang, W. Guo, Y. Wen, L. Wang, Y. Wang, R. Lin, T. Li, H. Tan, H. Peng, B. Zhang, Polymer-supported liquid layer electrolyzer enabled electrochemical CO_2 reduction to CO with high energy efficiency, ChemistryOpen 10 (2021) 639–644.

[47] W. Ren, X. Tan, C. Jia, A. Krammer, Q. Sun, J. Qu, S.C. Smith, A. Schueler, X. Hu, C. Zhao, Electronic regulation of nickel single atoms by confined nickel nanoparticles for energy-efficient CO_2 electroreduction, Angew. Chem. Int. Ed. Engl. 61 (2022) e202203335.

[48] Z. Yin, H. Peng, X. Wei, H. Zhou, J. Gong, M. Huai, L. Xiao, G. Wang, J. Lu, L. Zhuang, An alkaline polymer electrolyte CO_2 electrolyzer operated with pure water, Energy Environ. Sci. 12 (2019) 2455–2462.

[49] X. Rong, H.J. Wang, X.L. Lu, R. Si, T.B. Lu, Controlled synthesis of a vacancy-defect single-atom catalyst for boosting CO_2 electroreduction, Angew. Chem. Int. Ed. Engl. 59 (2020) 1961–1965.

[50] J. Zhao, S. Shahgaldi, X. Li, Z. Liu, Experimental observations of microstructure changes in the catalyst layers of proton exchange membrane fuel cells under wet-dry cycles, J. Electrochem. Soc. 165 (2018) F3337–F3345.

[51] N. Karst, V. Faucheux, A. Martinent, P. Bouillon, J.-P. Simonato, Improvement of water management in polymer electrolyte membrane fuel cell thanks to cathode cracks, J. Power Sources 195 (2010) 5228–5234.

[52] S. Vierrath, F. Güder, A. Menzel, M. Hagner, R. Zengerle, M. Zacharias, S. Thiele, Enhancing the quality of the tomography of nanoporous materials for better understanding of polymer electrolyte fuel cell materials, J. Power Sources 285 (2015) 413–417.

[53] F. Hegge, R. Moroni, P. Trinke, B. Bensmann, R. Hanke-Rauschenbach, S. Thiele, S. Vierrath, Three-dimensional microstructure analysis of a polymer electrolyte membrane water electrolyzer anode, J. Power Sources 393 (2018) 62–66.